The Astrophysical Journal, 927:12 (18pp), 2022 March 1 https://doi.org/10.3847/1538-4357/ac45fb

Long-term Photometric and Low-resolution Spectroscopic Analysis of Five Contact Binaries

A. Panchal[1,2], Y. C. Joshi[1], Peter De Cat[3], and S. N. Tiwari[2]
[1] Aryabhatta Research Institute of observational sciencES (ARIES), Nainital, Uttrakhand, India; alaxender@aries.res.in
[2] Department of Physics, DDU Gorakhpur University, Gorakhpur, India
[3] Royal Observatory of Belgium, Ringlaan 3, B-1180 Brussel, Belgium
Received 2021 September 16; revised 2021 December 20; accepted 2021 December 20; published 2022 March 2

Abstract

A photometric and spectroscopic investigation is performed on five W Ursae Majoris eclipsing binaries J015818.6+260247 (hereinafter as J0158b), J073248.4+405538 (hereinafter as J0732), J101330.8+494846 (hereinafter as J1013), J132439.8+130747 (hereinafter as J1324), and J152450.7+245943 (hereinafter as J1524). The photometric data are collected with the help of the 1.3 m Devasthal Fast Optical Telescope, the 1.04 m Sampurnanand Telescope, and the Transiting Exoplanet Survey Satellite space mission. The low-resolution spectra of the 4 m Large Sky Area Multi-Object Fiber Spectroscopic Telescope are used for spectroscopic analysis. The orbital period change of these systems is determined using our photometric data and previously available photometric data from different surveys. The orbital period of J1013 and J1524 is changing at a rate of $-2.552\ (\pm 0.249) \times 10^{-7}$ days yr^{-1} and $-6.792(\pm 0.952) \times 10^{-8}$ days yr^{-1}, respectively, while others do not show any orbital period change. The orbital period change of J1013 and J1524 corresponds to a mass transfer rate of 2.199×10^{-7} and $6.151 \times 10^{-8}\ M_{\odot}$ yr^{-1} from the primary to the secondary component in these systems. It is likely that angular momentum loss via magnetic braking may also be responsible for the observed orbital period change in the case of J1524. All systems have a mass ratio lower than 0.5, except J0158b with a mass ratio of 0.71. All the systems are shallow-type contact binaries. J0158b and J1524 are subtype A while others are subtype W. The H_{α} emission line region is compared with template spectra prepared using two inactive stars with the help of the STARMOD program. The J0158, J1324, and J1524 systems show excess emission in the residual spectra after subtraction of the template.

Unified Astronomy Thesaurus concepts: Eclipsing binary stars (444); Contact binary stars (297); Photometry (1234); Spectroscopy (1558)

Supporting material: machine-readable table

1. Introduction

W Ursae Majoris eclipsing binaries (EWs) are contact binaries in which both components are dwarf stars with the spectral class ranging from F–K. They show almost the same size primary and secondary minima (Kuiper 1941; Lucy 1967, 1968). Both components fill their Roche lobes and show strong tidal interaction. The contact binary systems are quite common. Out of the ∼2,083,548 confirmed variable stars in the VSX catalog (Watson et al. 2006), almost 25% are reported as contact binaries and ∼19% as EWs. As both components have a common convective envelope around them, change and/or loss in mass and angular momentum can take place (Lucy 1967, 1968; van't Veer & Maceroni 1989; Qian 2001). An orbital period change can be associated with mass transfer, angular momentum loss due to magnetic activities, or a light-time effect because of the presence of third component. Actually, angular momentum loss itself is the leading mechanism behind the formation of EWs from small period detached eclipsing binaries (DEBs). The evolution process is directed by the expansion of the most evolved component accompanied by mass transfer and angular momentum loss due to stellar wind, a third body, and/or mass loss. So DEBs can evolve to EWs via angular momentum loss (due to magnetic activities), third components (via Kozai cycles), or an evolutionary expansion of its components (Kozai 1962; van't Veer & Maceroni 1989; Li et al. 2004, 2007; Eker et al. 2008). Uneven-sized maxima are very common in photometric light curves (LCs) of EWs. Cool and/or hot spots are believed to be the reason behind this asymmetry of their LCs. Many EWs show excess or filled-in emission in their spectra due to magnetic activities (Barden 1984; Huenemoerder & Ramsey 1984; Montes et al. 1995). Due to the small separation of the components and the corresponding short orbital periods, these systems can be easily observed with ground-based telescopes on a short timescale. EWs are also appropriate targets to study many other processes like the O'Connell effect (O'Connell 1951), energy exchange between components, magnetic activity, orbital period changing mechanisms, thermal relaxation oscillation, etc. Photometric and spectroscopic data are essential for an accurate determination of the physical parameters of EWs.

In the present work, five EWs are analyzed and their absolute parameters, rate of orbital period change, and mass transfer, emission properties are studied. The system J1524 was first identified as a contact binary by the Robotic Optical Transient Search Experiment (ROTSE) survey (Akerlof et al. 2000). The other systems were classified as EWs by the Catalina Surveys Periodic Variable Star Catalog, which provides the average *V*-band magnitude, amplitude of variation, and period of periodic

Table 1
Basic Information about the Sources Taken from Different Surveys.

Source	R.A. (J2000)	Decl. (J2000)	Period (day) (1)	V (mag) (1)	A_V (mag) (2)	J-K (mag) (3)	Parallax (mas) (4)
J0158b	01:58:18.6	+26:02:47	0.263009	13.60	0.240	0.305	2.0283
J0732	07:32:48.4	+40:55:38	0.286025	14.61	0.151	0.668	1.0452
J1013	10:13:30.8	+49:48:46	0.250206	13.72	0.019	0.494	2.5813
J1324	13:24:39.8	+13:07:47	0.266082	13.59	0.060	0.494	1.9923
J1524	15:24:50.7	+24:59:43	0.244760	13.67	0.114	0.593	2.1804

References. (1) Drake et al. (2014); (2) Schlafly & Finkbeiner (2011); (3) Skrutskie et al. (2006) (2MASS survey); (4) Gaia Collaboration et al. (2021) (GAIA).

variables. The first data release of the Catalina Surveys identified ∼47,000 periodic variables among 5.4 million candidate stars within a 20,000 deg^2 region of sky (Drake et al. 2014). The objects J015818.6+260247 (J0158b), J073248.4+405538 (J0732), J101330.8+494846 (J1013), J132439.8+130747 (J1324), and J152450.7+245943 (J1524) are EWs, with an average *V*-band magnitude ranging from 13.5–14.5 and an orbital period ranging from 0.244–0.286 day in the Catalina Real-time Transient Survey (CRTS) Catalog. The basic information about the targets is listed in Table 1.

2. Observations

2.1. Photometry

For the photometric observations, we used the 1.3 m Devasthal Fast Optical Telescope (DFOT) and the 1.04 m Sampurnanand Telescope (ST), operated by the Aryabhatta Research Institute of Observational Sciences (ARIES). The DFOT has a 2k × 2k CCD with a ∼18′ × 18′ field of view (FoV). The DFOT CCD is operated with a gain of 2 e$^-$ ADU^{-1} and readout noise of 7.5 e$^-$. The ST is equipped with a 4k × 4k CCD with a FoV of ∼15′ × 15′. The ST CCD is used in 4 × 4 binning mode with a gain of 3 e$^-$ ADU^{-1} and readout noise of 10 e$^-$. Table 2 shows the observation log of DFOT and ST photometric observations. For the preprocessing of raw images, IRAF[4] routines were used. The standard procedure of bias subtraction, flat-fielding, and cosmic-ray removal was followed. The instrumental magnitudes were determined through aperture photometry using DAOPHOT (Stetson 1992). The differential LCs were generated after choosing suitable comparison stars close to the target stars in the field.

We also used the photometric observations by the Transiting Exoplanet Survey Satellite (TESS). TESS was launched in 2018 in search of exoplanets with sizes in the range between earth-like planets and gas giants. It is an all-sky survey that uses four cameras with a FoV of 24° × 24° each as back-end instruments. These cameras are combined to observe sectors of 24° × 96°. For the prime mission (first 2 yr), the region of the sky with an ecliptic latitude $|b| > 6°$ was divided into 26 different sectors to observe each of them for 27 days (Ricker et al. 2015). During this period, TESS observed 200,000 preselected targets with a 2 minute cadence while all the objects on the full frame images (FFIs) have an observation cadence of 30 minutes. TESS is now in the extended phase where large parts of the both ecliptic hemispheres are being reobserved but also attention is given to the region near the ecliptic equator. In this phase, the cadence of the FFIs has been increased to 10 minutes. The TESS data are publicly available at the the Barbara A. Mikulski Archive for Space Telescopes (MAST) portal.[5] The data products are available in the form of FFIs, target pixel files (TP; time series for calibrated pixels saved at a 2 minute cadence), and LV files (LC; flux time series determined from the TP files). In the LC files, the simple aperture photometry flux (SAP_FLUX) and detrended flux (PDCSAP_FLUX) is available. We used the PDCSAP_FLUX during the analysis as it was derived after removing effects of nearby stars and other systematic trends.

The photometric data from other surveys were also used for period analysis but most of the times of minima (TOMs) were derived from SuperWASP (Wide Angle Search for Planets) data. The SuperWASP project is an ultra-wide-angle photometric survey observing the northern and southern hemispheres of the sky from the sites of La Palma, Canary Islands, and South African Astronomical Observatory Sutherland. Each site covers almost a 500 deg^2 part of the sky with the help of eight cameras. The aperture size of each camera is 11.1 cm and uses a 2K × 2K EEV CCD. The FoV of an individual camera is around 7.8 × 7.8 deg^2 with a plate scale of 13.″7 per pixel (Pollacco et al. 2006). The individual object coordinates or IDs can be used for query on the SuperWASP public archive.[6] The archive contains time series data of almost 18 million targets observed during the SuperWASP survey.

2.2. Spectroscopy

The Large sky Area Multi-Object Fiber Spectroscopic Telescope (LAMOST) survey provides a huge collection of low-resolution spectra ($R \sim 1800$) of stars, galaxies, quasars, and other unknown objects. The multifiber design allows observation of 4000 targets simultaneously (Luo et al. 2015). Since the start of the second phase of the regular survey in 2018 September, the medium-resolution spectra ($R \sim 7500$) are also gathered. The second version of the 4th data release of the LAMOST survey includes 1,551,394 star spectra, 39,498 galaxy spectra, and 13,954 quasar spectra. The available low-resolution data of targets were downloaded from the LAMOST DR4 v2 website.[7] Table 3 provides an overview of these observations and the published values of the spectral subclass and stellar parameters (effective temperature $T_{\rm eff}$, surface gravity $\log g$, and metallicity [Fe/H]), derived with the LAMOST Stellar Parameter Pipeline (LASP). LASP uses the ULySS package for estimating temperature and other stellar

[4] IRAF is distributed by the National Optical Astronomy Observatory, which is operated by the Association of Universities for Research in Astronomy under cooperative agreement with the National Science Foundation.

[5] https://mast.stsci.edu
[6] https://wasp.cerit-sc.cz/form
[7] http://dr4.lamost.org/

Table 2
The 1.3 m DFOT and 1.04 m ST Observation Log

Date of Obs.	Start JD (2450000+)	End JD (2450000+)	Total Frames	Exposure Time (s)	Obs. Time (hr)
			V, R_c, I_c		
			J0158b		
2018-10-11	8403.4153	8403.4265	02, 02, 02	180,120,80	0.27
2018-11-20	8443.0701	8443.3544	51, 51, 50	120, 60,50	6.82
2018-12-27	8480.1347	8480.1715	06, 06, 06	180,120,80	0.88
2019-10-14	8771.1721	8771.4613	84, 84, 84	40, 25,20	6.94
2020-10-14	9137.3781	9137.4570	120, −, 140	20, −,20	6.94
2020-10-15	9138.3428	9138.4379	100, 100, −	30, 30,−	2.28
			J0732		
2021-02-25	9271.0616	9271.3119	38, 38, 38	120,120,120	6.01
2021-02-27	9273.0622	9273.3219	40, 40, 40	120,120,120	6.23
2021-03-01	9275.0603	9275.2778	75, 75, 75	60, 60, 60	5.22
2021-03-26	9300.0706	9300.2491	26, 28, 20	60, 60, 60	4.28*
2021-03-28	9302.1333	9302.2521	15, 19, 08	90, 90, 90	2.85*
2021-03-29	9303.0723	9303.1853	37, − , −	120, − , −	2.71*
2021-04-06	9311.0651	9311.1133	12, 12, 12	60, 60, 60	1.16*
2021-04-08	9313.0745	9313.1281	−, − , 27	−, − , 60	1.29*
			J1324		
2021-01-29	9244.3259	9244.5367	38, 37, 37	120, 80, 80	5.06
2021-01-30	9245.3338	9245.5395	37, 36, 36	120, 80, 80	4.94
2021-02-11	9257.4633	9257.5193	30, − , −	150, − , −	1.34
2021-02-17	9263.4822	9263.5245	30, − , −	120, − , −	1.01
2021-03-26	9300.2607	9300.5029	73, 73, 73	60, 60, 60	5.81*
			J1013		
			B, V, I_c		
2019-03-19	8562.2631	8562.2882	−, 05, 05	−,120, 60	0.60
2019-03-20	8563.2192	8563.2279	−, 02, 02	−,120, 60	0.21
2020-04-06	8946.1182	8946.2560	19, 19, 21	150,120, 60	3.31
2020-04-08	8948.0701	8948.2594	27, 27, 27	150,120, 60	4.54
2020-04-19	8959.1740	8959.2160	06, 07, 06	150,120, 60	1.01
2020-04-22	8962.1405	8962.2510	22, 22, 22	90, 60, 30	2.65
2020-11-07	9161.4246	9161.5170	−, 81,−	−, 60,−	2.22
2020-11-08	9162.4754	9162.4975	−, 30,−	−, 60,−	0.53
2020-11-14	9168.4224	9168.4982	−, 100, −	−, 60,−	1.82
2021-03-21	9295.1523	9295.1905	35, − , −	90, − , −	0.92
2021-03-27	9301.1317	9301.3740	46, 36, 47	150, 90, 60	5.81*
2021-03-28	9302.2724	9302.3657	51, − , −	150, − , −	2.24*
2021-03-29	9303.2060	9303.3640	39, 40, 39	60, 60, 60	3.79*
2021-03-30	9304.0771	9304.3503	49, 46, 48	180, 90, 60	6.56*
			J1524		
2018-05-25	8264.1858	8264.3735	15, 15, 16	300,180, 60	4.50
2018-05-26	8265.1056	8265.1889	09, 09, 09	300,150, 60	2.00
2019-03-15	8558.4717	8558.5088	06, 06, 06	200,150, 60	0.89
2019-03-19	8562.4843	8562.5079	04, 03, 03	200,150, 60	0.57
2019-03-21	8564.2599	8564.3224	08, 09, 09	200,150, 60	1.50
2019-03-28	8571.3943	8571.4934	18, 18, 18	120, 60, 30	2.38
2019-03-31	8574.4320	8574.4641	05, 05, 05	150,100, 60	0.77
2019-05-18	8622.3634	8622.4269	14, 07, 07	150,100, 80	1.53
2019-05-19	8623.2524	8623.3421	13, 13, 13	150,100, 80	2.15
2020-03-28	8937.4586	8937.4969	08, 08, 11	60, 40, 30	0.92
2020-03-29	8938.3352	8938.4886	35, 35, 35	60, 40, 30	3.68
2020-04-19	8959.4248	8959.4763	08, 08, 09	120, 90, 60	1.23
2020-04-21	8961.2938	8961.4712	16, 16, 16	90, 60, 30	4.26
2021-03-27	9301.4126	9301.5016	−, 114, −	−, 60,−	2.13
2021-03-28	9302.3826	9302.4914	59, − , −	150, − , −	2.61

Note. The "*" at the end of rows indicate the 1.04 m ST data.

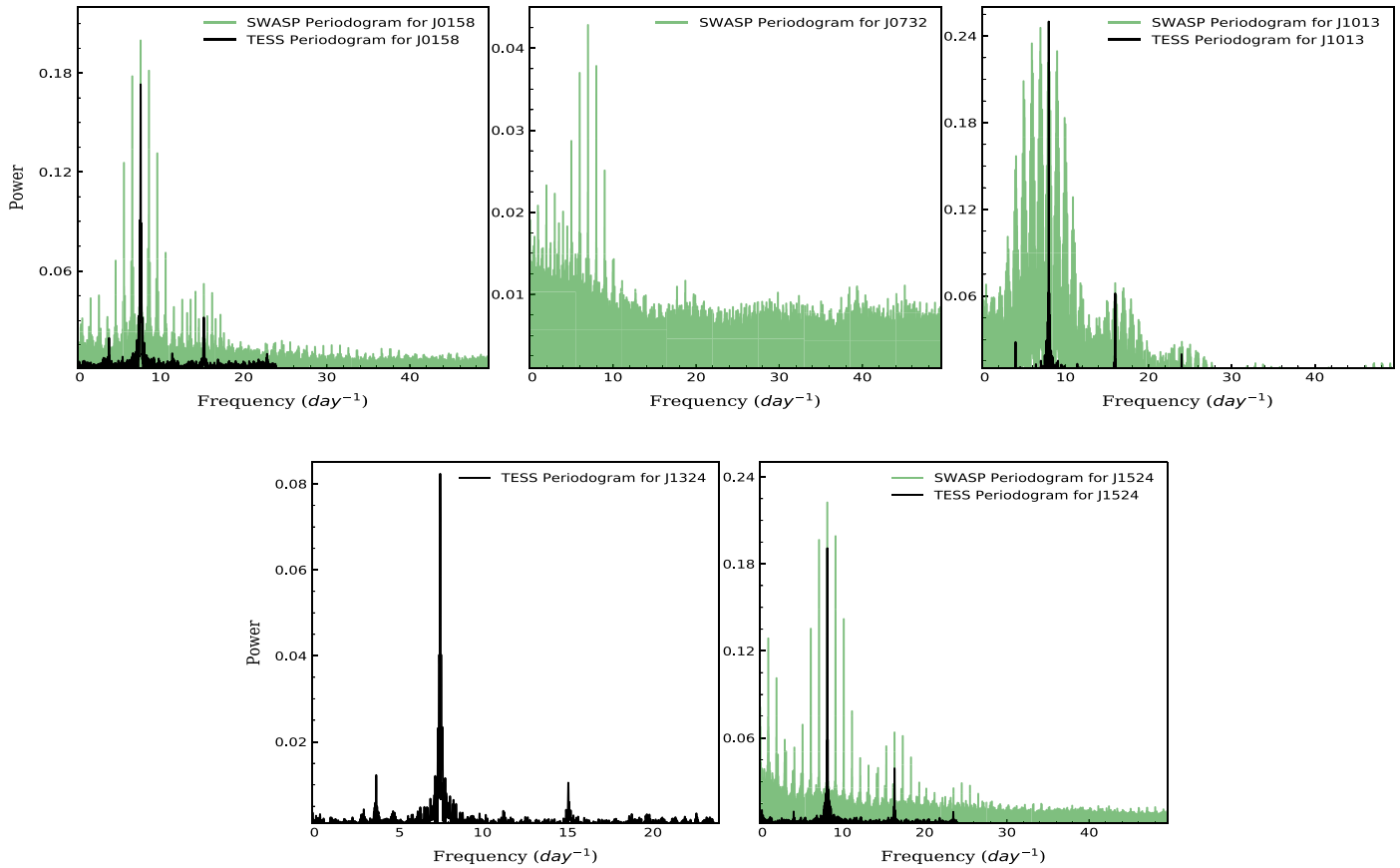

Figure 1. Power spectra obtained by applying the PERIOD04 software to the SuperWASP (light green) and TESS (black) data of the targets. The object names are given at the top right corner of each plot.

Table 3
Parameters of Targets as Listed in the Catalog Stellar Parameters of Low-resolution LAMOST Spectra (DR6 v2)

Targets	Date	$T_{\rm eff}$ (K)	Subclass	log g	[Fe/H] (dex)	S/N$_i$
J0158b	31-10-2013	5599(26)	G7	4.35(4)	−0.34(3)	144
	31-10-2013	5316(33)	G7	3.95(6)	−0.50(3)	138
	08-12-2014	5562(17)	G7	4.28(3)	−0.35(2)	274
J0732	07-03-2015	5494(183)	G7	4.16(19)	−0.27(19)	77
J1013	23-01-2013	4926(140)	K3	4.57(18)	−0.03(13)	50
	05-02-2015	⋯	⋯	⋯	⋯	12
J1324	18-01-2012	4997(58)	K1	4.60(10)	−0.32(6)	103
J1524	12-03-2016	5198(22)	G7	4.00(4)	−0.71(2)	173

Note. The errors in the units of the last decimal are given between parentheses.

parameters from the observed spectra. The stellar spectra are compared with similar resolution model spectra to minimize the χ^2 (Luo et al. 2015). S/N$_i$ denotes the signal-to-noise ratio in the Sloan i band. All targets are classified as main-sequence late-type objects.

3. Orbital Period and Orbital Period Change

We analyzed the time series for these objects in order to detect any secular changes in their orbital period $P_{\rm orb}$. The period analysis is an effective way for understanding processes like mass loss/transfer, long-term activity cycles, the influence of a third component, and the dynamical evolution of eclipsing binaries. Accurate $P_{\rm orb}$ values were determined by applying the PERIOD04 software (Lenz & Breger 2004, 2005) to the SuperWASP and TESS data of the targets. This software can handle time series with large gaps and multiperiodic signals. SuperWASP data are available for J0158b, J0732, J1013, and J1524 while the TESS mission observed all the targets except J0732. These targets were also observed in many other surveys but due to the large time span and better cadence of SuperWASP and TESS data, only these surveys data were used to determine period. The power spectra that were used for the period search are shown in Figure 1. The SuperWASP data power spectra for J0158b,J0732, J1013, and J1524 show peak

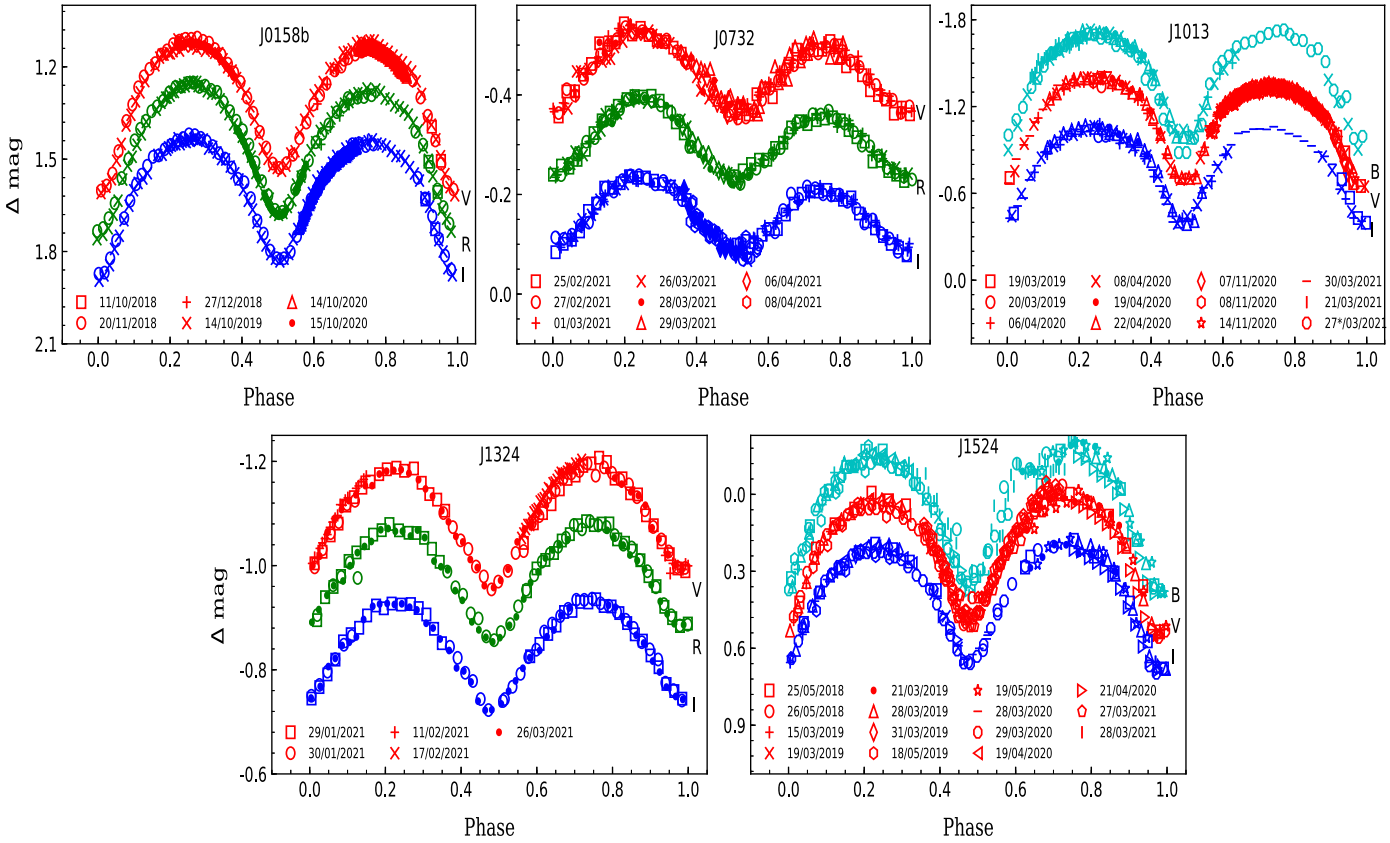

Figure 2. The multiband LVs of the five targets observed using the 1.3 m DFOT and 1.04 m ST. The different colors represent different bands also mentioned in the right side of each plot. The different symbols correspond to different dates of observations.

at frequencies 7.604314(4), 6.99249(4), 7.9934(2), and 8.17127(8) day^{-1}, respectively. The power spectra derived from TESS data show peak at frequencies 7.6036(2), 7.9932 (2), 7.5163(2), and 8.1721(1) for J0158b, J1013, J1324, and J1524, respectively. The primary and secondary minima are almost indistinguishable due to nearly equal depths, so, the periods ($1/\mathrm{freq_{peak}}$) given by a periodogram are half of the actual period, i.e., $2/\mathrm{freq_{peak}}$. The periods are determined as 0.263033(7), 0.250213(6), 0.266088(7) and 0.244735(3) day for J0158b, J1013, J1324, and J1524, respectively, from the TESS photometric time series. The periods from SuperWASP data are found to be 0.2630086(1), 0.286021(2), 0.250206(6), and 0.244759(2) for J0158b, J0732, J1013, and J1524, respectively. The periods obtained from SuperWASP and TESS are very close to the previously reported values in Drake et al. (2014). The phase-folded observed LCs derived from estimated periods in different photometric bands are shown in Figure 2.

The change in orbital period with time is investigated by studying the variations in time of minima (TOMs) at different epochs. For this, we used data from different surveys such as the CRTS, SuperWASP (Butters et al. 2010), Zwicky Transient Facility (ZTF; Bellm 2014; Ofek et al. 2020), Palomar Transient Factory (PTF; Ofek et al. 2012), TESS, and 1.3 m DFOT observations. For SuperWASP, there was a small shift in the observed magnitudes corresponding to different SuperWASP cameras on some specific days of observations. We therefore separated all data points according to camera ID, e.g., all data points observed using camera-101 in one file, camera-102 in other file, and so on. Each night LCs were plotted using these data files prepared on the basis of camera IDs. We visually analyzed the LC of each individual night and only selected the good quality LCs for the TOM determination (LCs with less scattering and covering at least >50% part of the phase around one of the minima). In some cases, one of the minima was observed but the number of data points was small around the minima region and not enough for TOM determination using parabola fitting. In these cases, data from consecutive days were combined together to get a combined LC with good number of data points in the minima region. The TOM was determined by parabola fitting to the data around primary or secondary minima. A similar procedure was used to determine TOM for data collected from other surveys. In the following subsections, we describe the orbital period change analysis based on these TOMs for each target individually.

3.1. J0158b

The three TOMs were determined using SuperWASP photometric observations. The observations by CAM-101 from JD 2453229–2453237, CAM-141 from JD 2453970–2453972 and CAM-142 from JD 2453979–2453998, were combined together to calculate two primary and one secondary TOMs. A total of three secondary minima were calculated from CRTS data (data of 80–100 days was combined for generating LCs). We also determined 16 TOMs from TESS data and five TOMs from DFOT data. The $O-C$ was calculated using an orbital period of 0.263009 day. The linear ephemeris was computed by line fitting to the orbital cycle-TOM curve, which can be

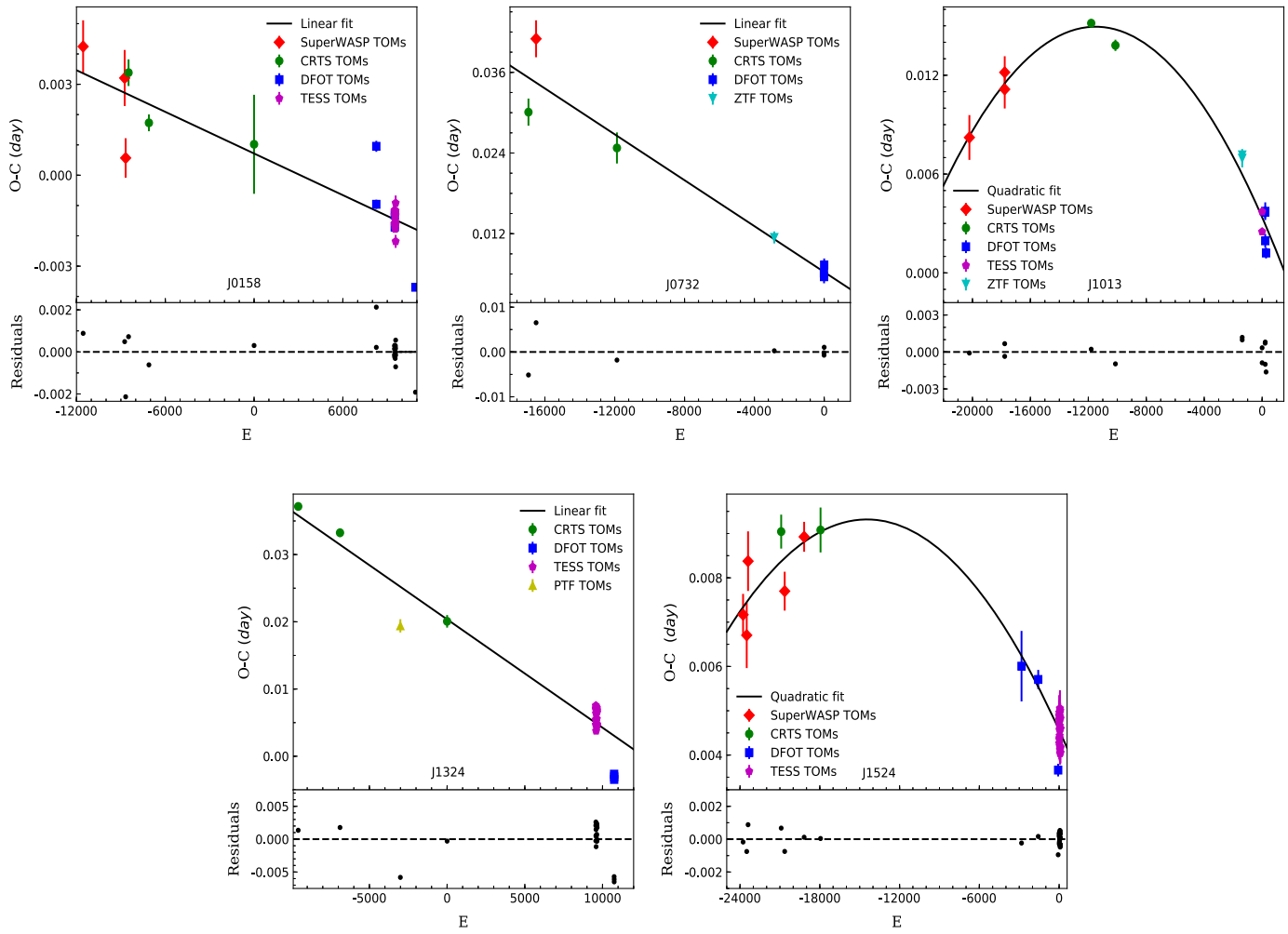

Figure 3. The $O-C$ diagrams of the targets with a linear/quadratic fit. The x-axis corresponds to the orbital cycle number and y-axis represents the $O-C$ difference in TOMs. The residuals of the fit are shown in lower subpanels. The target name is listed in each plot.

expressed as

$$\mathrm{HJD}_o = 6271.233769(\pm 0.000198) + 0.26300877 (\pm 0.00000002) \times E. \quad (1)$$

Here, HJD_o represents ($\mathrm{HJD}_{\mathrm{TOM}}$-2,450,000) at the primary minimum of orbital cycle number E. The top left panel of Figure 3 shows the best-fitted line to the E versus $(O-C)$ plot. The lower part shows the residuals of the fit. The fitted line can be represented by

$$O - C = 0.0007(\pm 0.0002) - 2.2901(\pm 0.2148) \times 10^{-7} \times E. \quad (2)$$

The TOMs from SuperWASP and CRTS show larger error bars as compared to those from TESS and DFOT data TOMs because of the quality of photometric observations. From the top left panel of Figure 3, we conclude that there is no evidence for a change of the P_{orb} value of J0158b in the time span of the photometric observations that were used in the present study.

3.2. J0732

J0732 is the only system in our sample for which no TESS data is available. A total of seven TOMs (one from CRTS, two from SuperWASP, one from ZTF, and three from DFOT data) were evaluated for J0732. The updated ephemeris was found to be

$$\mathrm{HJD}_o = 9275.20879(\pm 0.00199) + 0.2860233 (\pm 0.0000002) \times E. \quad (3)$$

Similar to the J0158b system, the $O-C$ variation with E can be represented by a straight line. The fitted line is shown in the top middle panel of Figure 3 and defined as

$$O - C = 0.006(\pm 0.002) - 1.7065(\pm 0.1981) \times 10^{-6} \times E. \quad (4)$$

Since this system also shows linearity in the $O-C$ diagram, we can say its period remained constant for the last 13 yr.

3.3. J1013

For J1013, 13 TOMs were calculated (three from SuperWASP, two from CRTS, two from ZTF, two from TESS, and four using DFOT data). The linear ephemeris for J1013 follows the equation

$$\mathrm{HJD}_o = 8894.309(\pm 0.001) + 0.2502052 (\pm 0.0000001) \times E. \quad (5)$$

Table 4
Eclipse Minima Timings for J0158b, J0732, J1013, J1324, and J1524

ID	HJD_o (2450000+)	Min	Cycle	$(O-C)_1$ (days)	$(O-C)_2$ (days)	References
J0158b	3233.220340(864)	p	−11551	0.004246	0.000884	1
J0158b	3971.091050(925)	s	−8745.5	0.003207	0.000487	1
J0158b	⋯	s	⋯	⋯	⋯	⋯
J0158b	⋯	s	⋯	⋯	⋯	⋯
J0732	8457.325452(893)	s	−2859.5	0.011446	0.000265	5
J0732	9275.209839(968)	p	0.0	0.007345	0.001044	3
J0732	⋯	s	⋯	⋯	⋯	⋯
J0732	⋯	s	⋯	⋯	⋯	⋯
J1013	8550.278425(558)	s	−1375.0	0.006963	0.000981	5
J1013	8550.403730(269)	p	−1374.5	0.007166	0.001184	5
J1013	⋯	s	⋯	⋯	⋯	⋯
J1013	⋯	s	⋯	⋯	⋯	⋯
J1324	3835.832758(471)	p	−9580.5	0.037157	0.001352	2
J1324	4551.589427(623)	p	−6890.5	0.033246	0.001776	2
J1324	⋯	s	⋯	⋯	⋯	⋯
J1324	⋯	s	⋯	⋯	⋯	⋯
J1524	8956.458941(457)	p	0.0	0.004895	0.000333	4
J1524	8970.288040(362)	p	56.5	0.005054	0.000529	4
J1524	⋯	s	⋯	⋯	⋯	⋯
J1524	⋯	s	⋯	⋯	⋯	⋯

Note. Here 1–6 show TOMs obtained by SuperWASP, CRTS, DFOT, TESS, ZTF, and PTF. This is only sample table and the full table is only available in the online version of the paper.

(This table is available in its entirety in machine-readable form.)

The updated quadratic ephemeris for J1013 can be represented by

$$\mathrm{HJD}_o = 8894.3077(\pm 0.0003) + 0.2502037(\pm 0.0000001) \times E - 8.745(\pm 0.852) \times 10^{-11} \times E^2. \quad (6)$$

The nonlinear variation is obvious in the $O-C$ diagram shown in the bottom left panel of Figure 3. The $O-C$ variations are best fitted with the following quadratic expression:

$$O - C = 0.00338(\pm 0.00036) - 2.01119(\pm 0.15641) \times 10^{-6} \times E - 8.746(\pm 0.852) \times 10^{-11} \times E^2. \quad (7)$$

The nonlinear $O-C$ variations of J1013 are due to a change in its orbital period at a rate of $-2.552(\pm 0.249) \times 10^{-7}$ days yr^{-1}.

3.4. J1324

J1324 was not observed in the SuperWASP survey. We determined a total of 26 TOMs (three using CRTS, one using PTF, 19 using TESS and three using DFOT data) for this system. The linear ephemeris is derived as follows:

$$\mathrm{HJD}_o = 6385.01457(\pm 0.00096) + 0.2660804 (\pm 0.0000001) \times E. \quad (8)$$

The $O-C$ variation with E shows a linear variation (see top right panel of Figure 3). The fitted line equation is expressed as

$$O - C = 0.0204(\pm 0.0009) - 1.611598(\pm 0.103038) \times 10^{-6} \times E. \quad (9)$$

As for the systems J0158b and J0732, this system also does not show any noticeable change in P_{orb}.

3.5. J1524

In addition to three DFOT TOMs, we determined five using SuperWASP, two using CRTS and 27 using TESS data for J1524. In totality, we used 38 eclipsing timings for analysis of J1524. From the estimated TOMs, the updated linear ephemeris is derived as

$$\mathrm{HJD}_o = 8956.4587(\pm 0.0001) + 0.24475983 (\pm 0.00000001) \times E. \quad (10)$$

The least-squares solution for quadratic ephemeris is given by

$$\mathrm{HJD}_o = 8956.45861(\pm 0.00007) + 0.24475934(\pm 0.00000007) \times E - 2.2773(\pm 0.3192) \times 10^{-11} \times E^2. \quad (11)$$

The $(O-C)$ diagram with residuals for J1524 is shown in the bottom right panel of Figure 3. A nonlinear $O-C$ variation with epochs is clearly noticeable in the diagram. A quadratic fit is drawn for this variation. The following equation represents the nonlinear behavior of $O-C$ for J1524:

$$O - C = -0.00456(\pm 0.00007) - 6.5818(\pm 0.7008) \times 10^{-7} \times E - 2.2773(\pm 0.3192) \times 10^{-11} \times E^2. \quad (12)$$

The shape of the $O-C$ curve is similar to a downward parabola as exhibited in case of J1524. The rate of orbital period change is calculated using Equation (12). The system shows period variation of $-6.792(\pm 0.952) \times 10^{-8}$ days yr^{-1}. Some of the TOMs for each target are listed in Table 4, which is a sample table.

Table 5
$T_{\rm eff}$ (in K) Determined from Different Empirical Relations and LAMOST data

J0158	J0732	J1013	J1324	J1524	Ref
5384(133)	5733(151)	4925(167)	5187(108)	5336(145)	1
5500(125)	5500(125)	5000(125)	5000(125)	5250(125)	2
5492(15)	5494(184)	4926(140)	4997(58)	5198(21)	3
5459(61)	5576(90)	4950(84)	5061(58)	5261(64)	4

Note. The entries in column "Ref" refer to different methods used to determine the $T_{\rm eff}$: 1 for the $(J-H)$–$T_{\rm eff}$ relation of Collier Cameron et al. (2007), 2 for SED fitting, 3 for the average of the values listed in LAMOST catalog, and 4 for the average of these values.

4. LC Modeling

The legacy version of PHOEBE-1.0 (PHysics Of Eclipsing BinariEs) was used for analysis of photometric LCs. The program is based on Wilson–Devinney code (Wilson & Devinney 1971). Due to the release of more advanced version PHOEBE 2 the legacy version of PHOEBE is not actively maintained. Although PHOEBE 2 is more precise having some new features but the legacy version is efficient and more tested than the new version. The legacy version provides a graphical user interface (GUI) and a scripter for fitting and reproducing LCs and radial velocity (RV) curves. The GUI helps analyze the reproduced LCs after each iteration and the scripter can be used for the analysis of large data sets. The PHOEBE scripter helps in the analysis as well as the statistical tests for the obtained results (Prša & Zwitter 2005). We used the differential corrections minimization method while modeling the targets. Depending upon the Roche lobe geometry (detached, semi-detached, or contact binary) of the system, different models can be selected in PHOEBE. Currently, there are eight models available in PHOEBE. We used the *over contact binary not in thermal contact* model for the initial estimate of parameters. This model assumes that the components are in geometrical contact but their temperature can be different. In this model, the secondary temperature is independent of the primary temperature. If the system under study is in thermal contact, then both models give the same results.

4.1. Effective Temperature

In the modeling process, we needed to fix some of the parameters like HJD_o, period, etc. The temperature of the primary and/or secondary component can be fixed provided a good estimate is available. The photometric results are not affected much by small changes in the temperature but fundamental parameters like luminosity of individual components, separation between components (which we will derive from the total luminosity), and the total mass of the system can be affected by the change in effective temperature. To get a better estimate of the temperature, we used two different methods for the calculation of $T_{\rm eff}$ in addition to the temperature estimates available in the LAMOST survey. First, we used the $(J-H)$–$T_{\rm eff}$ relation given by Collier Cameron et al. (2007) as the J and H-band magnitudes were available for all the sources from the Two Micron All Sky Survey (2MASS survey; Skrutskie et al. 2006; 1 in Table 5). In the second method, we collected all the publicly available photometric data in different bands and created the spectral energy distribution (SED) for each system. The $T_{\rm eff}$ was estimated

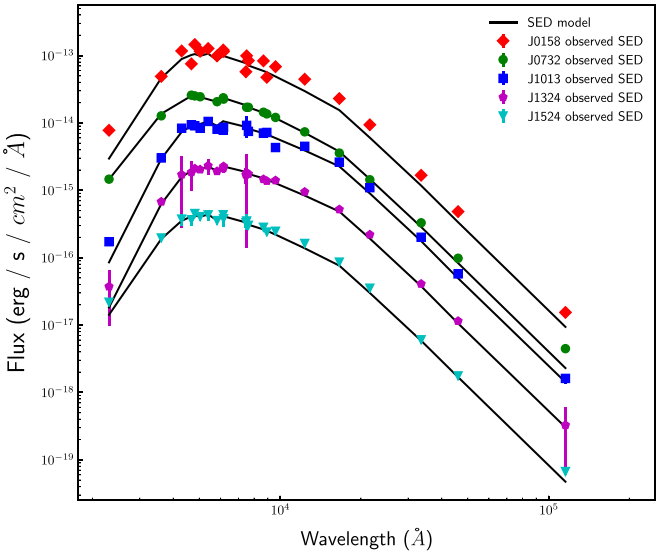

Figure 4. The generated SED and fitted curve for the five systems. A vertical shift is introduced while plotting to make every SED clearly visible.

with the help of VOSA SED fitter[8] (2 in Table 5). It is an automatic tool that provides access to different photometric catalogs, generates and fits the SED, estimates the luminosity, generates an H-R diagram, etc. The best-fit model is selected via χ^2 minimization. We used the $\log g$ and [Fe/H] values as listed in the LAMOST catalog. The Kurucz ODFNEW/NOVER model was used for SED fitting (Bayo et al. 2008). The fitted SEDs for all the sources are shown in Figure 4. The flux is shifted by some constant multiplication factor ($F_{J0158}\times 10$, $F_{J0732}\times 5$, F_{J1013}, $F_{J1324}\times 0.2$, and $F_{J1524}\times 0.04$) so that all the SEDs are clearly visible. The $T_{\rm eff}$values resulting from the SED fitting are 5500 (±125), 5500 (±125), 5000 (±125), 5000 (±125) and 5250 (±125) K for J0158b, J0732, J1013, J1324, and J1524, respectively (2 in Table 5). The Table 5 also includes the average $T_{\rm eff}$ values as listed in the LAMOST catalog (indicated with 3). We used the non-weighted mean of the three different $T_{\rm eff}$ estimates for each system (4 in Table 5) as effective temperature of the primary component ($T_1^{\rm eff}$) for the LC modeling. Note that the subscripts 1 and 2 are used throughout the paper to refer to the primary and secondary components, respectively.

4.2. LC Solution

These sources were not observed using high-resolution spectrographs in the past, so no information was available about their RV variations. As we have been carrying out the first detailed photometric analysis of these target stars, no earlier estimates of the mass ratio ($q=M_2/M_1$) were available in the literature. We derived q by applying the q-search technique on the available multiband photometric LCs (e.g., Joshi et al. 2016; Joshi & Jagirdar 2017). For the q search, only DFOT and ST data were used. All the multiband LCs from DFOT and ST were used at the same time for the q search. The orbital period, TOMs, $T_1^{\rm eff}$, gravity darkening coefficients ($g_1=g_2=0.32$), and bolometric albedos ($A_1=A_2=0.5$) were fixed while the effective temperature of the secondary component ($T_2^{\rm eff}$), surface potentials ($\Omega_1=\Omega_2$), luminosity of the primary component (L_1), and orbital inclination (i) were set

[8] http://svo2.cab.inta-csic.es/theory/vosa/

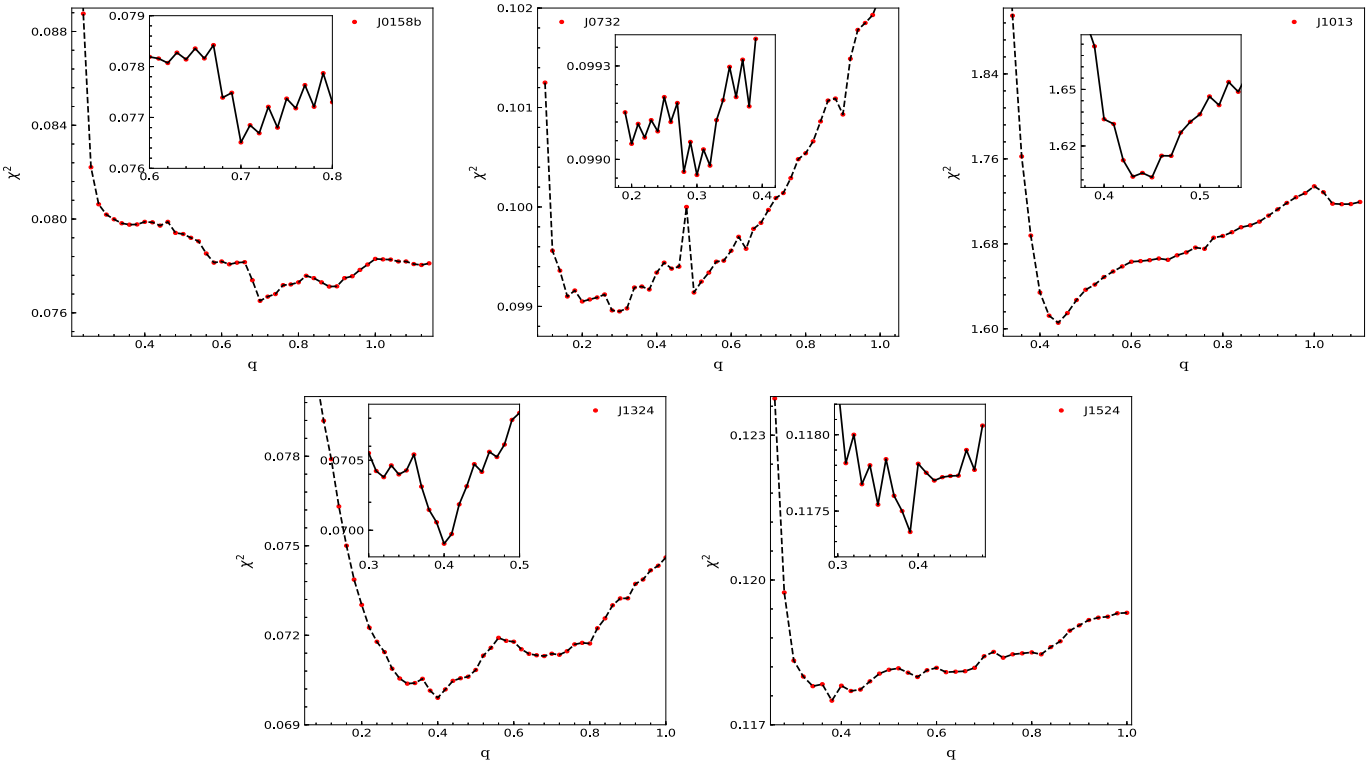

Figure 5. The variation of χ^2 for different values of the mass ratio q for J0158b (top left), J0732 (top middle), J1013 (top right), J1324 (bottom left), and J1524 (bottom right). A zoom-in of the region around the minimum χ^2 value with smaller increments of q (0.01) is given in the subpanels.

free. The eccentricity (e), rate of orbital period change, synchronicity parameters (F_1, F_2), and third light (l_3) were fixed to zero during analysis. The code automatically selects and modifies the limb darkening coefficients from the van Hamme (1993) tables after each iteration. While applying the q-search process, different models were created with mass ratios varying from 0.04 to higher values in small steps of 0.02. Following every 30 iterations, the parameter set was altered randomly by ±5% of their actual value. For each q value we used this random shift in parameters for 20 times. Therefore, every 600 (20×30) iterations gave the best-fit model for a given q input. It is expected that the residuals after subtraction of the synthetic LCs from the observed LCs would decrease as soon as the q would approach the true mass ratio. A q versus χ^2 plot is shown in Figure 5. The region around the minima is further explored with smaller step size of 0.01 as shown in the zoomed subpanels of Figure 5. As all the targets are EWs according to the CRTS catalog, we used the contact mode during the q search. On the basis of fill-out factor it was found that the system J1324 was on the edge of contact geometry. Therefore, the same procedure of the q search was repeated but this time with the semidetached mode. The semidetached mode gave a slightly better fit as compared to the contact mode (χ^2 decreased to 0.0399 from 0.0413) for J1324. Hence, for the J1324 analysis, the semidetached mode of PHOEBE was used. The initial estimates for q are 0.70(±0.02), 0.30(±0.01), 0.45 (±0.02), 0.40(±0.01), and 0.39(±0.02) for J0158b,J0732, J1013, J1324, and J1524, respectively. As the more massive component was considered as primary for all systems, the resulting q values were below 1. The mass ratio estimated using the q search and other parameters corresponding to that mass ratio are the initial estimates. To refine the model parameters and determine the uncertainties more robustly, a Markov Chain Monte Carlo (MCMC) technique was used. A python script that wraps PHOEBE and the EMCEE code by Foreman-Mackey et al. (2013) was used for this purpose (Prša & Zwitter 2005). EMCEE is a python-based sampler that uses MCMC methods that remain unaffected by affine tranformations (Goodman & Weare 2010). We adjusted five parameters, q, i, $T_2^{\rm eff}$, $\omega_{1/2}$, and L_1 during the MCMC run. The number of walkers were set to 100 and 5000 iterations were used. The parameters determined from the q search were used as priors. A boundary limit was used for all the five parameters. The chosen number of chains and iterations evaluated 500,000 models. We discarded first 10,000 iterations out of these 500,000 models. The output of initial chains was used as starting point for later iterations. The mean and the standard deviation were used as the final parameters and uncertainties. The temperature of secondary ($T_2^{\rm eff}$), surface potential of primary/secondary components ($\Omega_{1/2}$), inner/outer critical roche equipotential ($\Omega_{\rm in/out}$), luminosity ratio in different bands (L_1/L_T), relative radii of primary/secondary components ($r_{1/2}$) in units of semimajor axis, and fill-out factor (f) obtained from the LC modeling are given in Table 6.

The parameter space around the final solutions was also analyzed. The region around final parameters was divided into a grid and multiple iterations were used to find the minimum χ^2 for each point on this parameter grid (Prša & Zwitter 2005). Although different minimization techniques can give best solution for appropriately fed data sets after multiple iterations but sometimes a minimizer can be stuck in local minima also. As mentioned by Prša & Zwitter (2005), the global minima can have lots of local minima within itself as it is very flat. The parameter degeneracy and noise on the data points can make it difficult for the minimization techniques to converge the solution to the global minimum. Therefore, random ±5% kicks

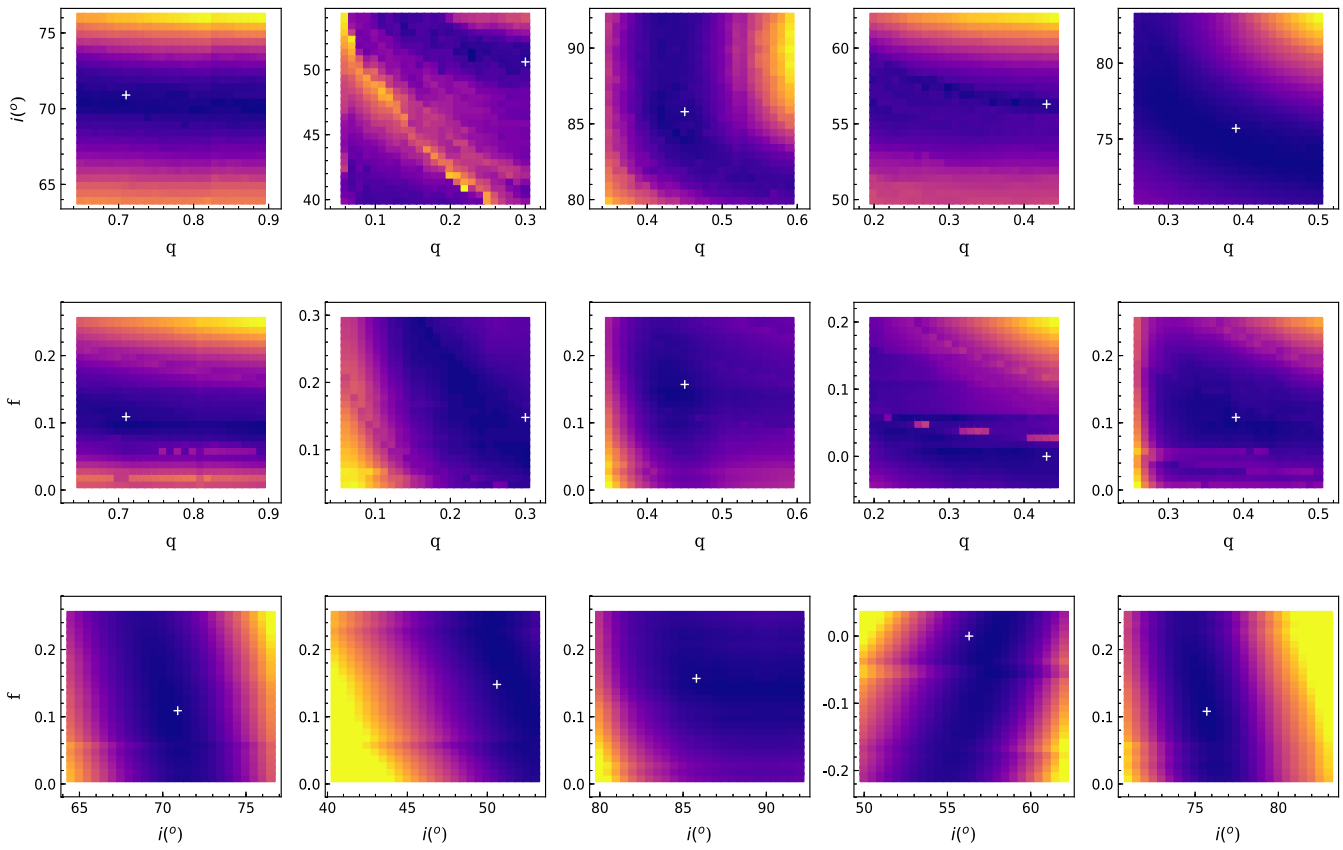

Figure 6. The *q–i*, *q–f*, and *i–f* parameter spaces around the adopted solutions (shown by the white "+" sign) for all the targets. The color yellow is used for the highest χ^2 values and blue for the lowest ones. The panels in Column 1–5 correspond to J0158b, J0732, J1013, J1324, and J1524, respectively.

Table 6
The LC Solution for Targets Derived Using DFOT and ST Observations

Parameters	J0158b	J0732	J1013	J1324	J1524
q	0.71(1)	0.296(15)	0.45(1)	0.43(1)	0.39(1)
i (°)	70.9(1)	50.6(2)	85.8(1)	57.4(1)	75.7(3)
$T_2^{\rm eff}/T_1^{\rm eff}$	0.95(1)	1.002(17)	1.01(2)	1.07(1)	0.98(1)
Ω_1	3.22(1)	2.44(1)	2.73(1)	2.74	2.63(1)
Ω_2	3.22(1)	2.44(1)	2.73(1)	2.72(2)	2.63(1)
L_1/L_T(B)	⋯	⋯	0.633	⋯	0.728
L_1/L_T(V)	0.643	0.755	0.658	0.596864	0.729
L_1/L_T(R)	0.630	0.753	⋯	0.610890	⋯
L_1/L_T(I)	0.614	0.745	0.659	0.611605	0.713
r_1	0.418	0.491	0.463	0.453383	0.471
r_2	0.361	0.289	0.321	0.309162	0.308
f(%)	10.9(2.5)	09.4(5.4)	15.7(3.7)	8.4(7.6)	10.8(4.2)

Note. For J1324 the fill-out factor of the secondary is given. The errors are in parentheses.

in the parameter values were applied after every 40 iterations with the help of PHOEBE scripter. These random kicks help to knock the solution parameter set out of local minima (if present) and facilitate the converging process to reach the global minima. The process helps increase the convergence efficiency of the minimization method. The 2D parameter space around the solutions in different combinations of (*q–i*), (*q–f*), and (*i–f*) are shown in Figure 6. Figure 6 shows the variation of χ^2 in the *q–i*, *q–f*, and *i–f* parameter spaces. The variation of color from yellow to blue in the Figure 6 shows changing χ^2. It is clearly visible that the adopted final solution falls in the bluer region of the parameter space and hence corresponds to the global minima region.

For J0158b, the components' temperature ratio ($T_2^{\rm eff}/T_1^{\rm eff}$) is ∼0.95. The secondary temperature is almost 266 K less than the primary temperature. The secondary minima are almost 0.07 mag dimmer than the primary minima. The primary component is bigger as well as hotter in this system, so it is essentially a subtype-A EW. As the model over contact not in thermal contact is used for the photometric LC analysis, the potential Ω of both the primary and secondary stars are kept the same ($\Omega_1 = \Omega_2$). They are found to be 3.22. The resulting fill-out factor f of 10.9% indicates that it is a shallow-contact-type system. The same q is used for the modeling of the TESS LC of J0158b. We used the same procedure and found a slightly different inclination i. The best-fit model of the TESS data has an orbital inclination and $T_2^{\rm eff}$ of 69°.24 and 5074 K, respectively.

For the system J0732, the amplitude of variation is 0.16 mag, which is smaller than that of the other targets. The mass ratio q is determined to be 0.296(±0.005) and the orbital inclination i is estimated to be 50.6(±0.2)°. Unlike J0158b, the secondary component in J0732 has an almost similar temperature to the primary component. The components' temperature ratio in this case is found to be 1.002. The fill-out factor f for this system is determined as 9.4%. The difference between the two maxima (around orbital phase 0.25 and −0.25) is visible in Figure 7. This difference is almost 0.03 mag. The brightness is expected to be equal around the phase −0.25 and 0.25 because the same amount of cross section is visible in both cases. This

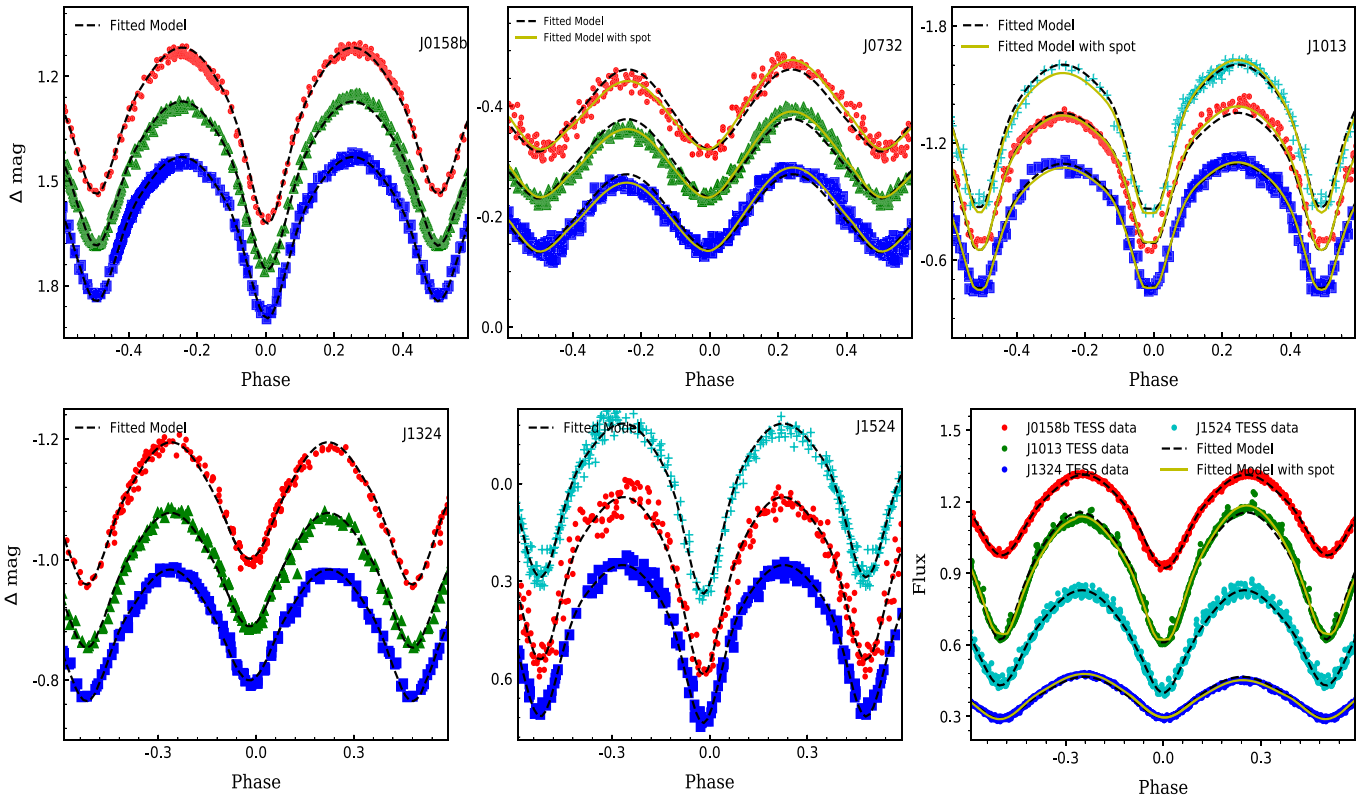

Figure 7. The synthetic LCs (black dashed lines for model without spot and yellow continuous for model with spot) are overplotted to the observed data in different bands as shown by cyan + marker (B), red dots (V), filled green triangles (R), and filled blue squares (I) dots. The last plot shows TESS observations' corresponding model generated synthetically and different colors indicate different targets.

asymmetrical behavior could originate from a spot on the surface of one of the components. In most of the cases, a time series of high-resolution spectra is required to map the surface of each component. This process is known as Doppler imaging. It helps determine the position, size, distribution, and motion of the spot. However, it is possible to determine accurate spot parameters solely based on photometric data with an accuracy of 0.1 mmag or better (Eker 1999). As the other system parameters could be affected by the use of incorrect spot parameters, they were fixed while determining the spot features through χ^2 minimization. We tried different positions for the cool/hot spot on the primary/secondary components and on the basis of minimum χ^2, the spot was placed at colatitude 45° and longitude 90° of the primary component. The temperature ratio and size were determined to be $0\overset{\circ}{.}83$ and 15°, respectively.

The system J1013 is a totally eclipsing binary system with an inclination of 85.76(±0.09)°. Both components have almost similar temperature: the components' temperature ratio is calculated as 1.01. The fill-out factor f is determined as 15.7%. This system also shows a difference in brightness at orbital phases −0.25 and 0.25. The system is ∼0.07 mag brighter at orbital phase 0.25. We tried a cool spot on secondary as well as a hot spot on the primary component but the hot spot on the primary component gave a better fit. Therefore, a hot spot was used on the primary component and placed at colatitude 86° and longitude 80°. The temperature ratio and size is determined to be $1\overset{\circ}{.}12$ and 17°, respectively. In case of the TESS data analysis, i and $T_2^{\rm eff}$ are determined as 86° and 5003 K, respectively. The luminosity ratio (L_1/L_T) in the TESS band is estimated as 0.651. The position of the hot spot is slightly different as determined using the TESS LC. The hot spot is estimated to be at colatitude 84° and longitude 71°, in the case of TESS data. The system shows subtype-W characteristics as the bigger component is cooler.

The system J1324 also has a low orbital inclination of 56.3 (±0.2)°. The temperature of the secondary component is higher than the primary component by ∼7%, i.e., nearly 334 K. J1324 is expected to be a semidetached system. The bigger component, i.e., the primary component of the system is cooler than the secondary component. Therefore, the system is classified as subtype W. As only a marginal asymmetry level is observed in the DFOT data (∼0.008 mag), no spot is used in the LC analysis. In the case of the TESS data, the asymmetry is larger. We therefore included a spot on the primary component in the modeling of the TESS LC, reducing the χ^2 from 0.076 to 0.023. The colatitude, longitude, radius, and temperature ratio are determined as 57°, 279°, 15° and $0\overset{\circ}{.}88$, respectively. While using the TESS LC, the components' temperature ratio is determined as 1.03. The $T_2^{\rm eff}$ estimated by TESS LC is ∼250 K below the $T_2^{\rm eff}$ value determined from the DFOT LCs.

For J1524, q and i are found to be $0\overset{\circ}{.}389$ and ∼76°, respectively. The primary component's temperature is hotter than the secondary component's temperature by 109 K. The J1524 system is a subtype-A system. The fill-out factor f is 10.8%. The secondary temperature is calculated as 5152 K using the TESS LC. With the TESS data, we find the orbital inclination as ∼74°. The parameters determined using the DFOT and ST photometric LCs are given in Table 6. The radii given in Table 6 are relative radii of the components in the unit of semimajor axis (A). They are determined by

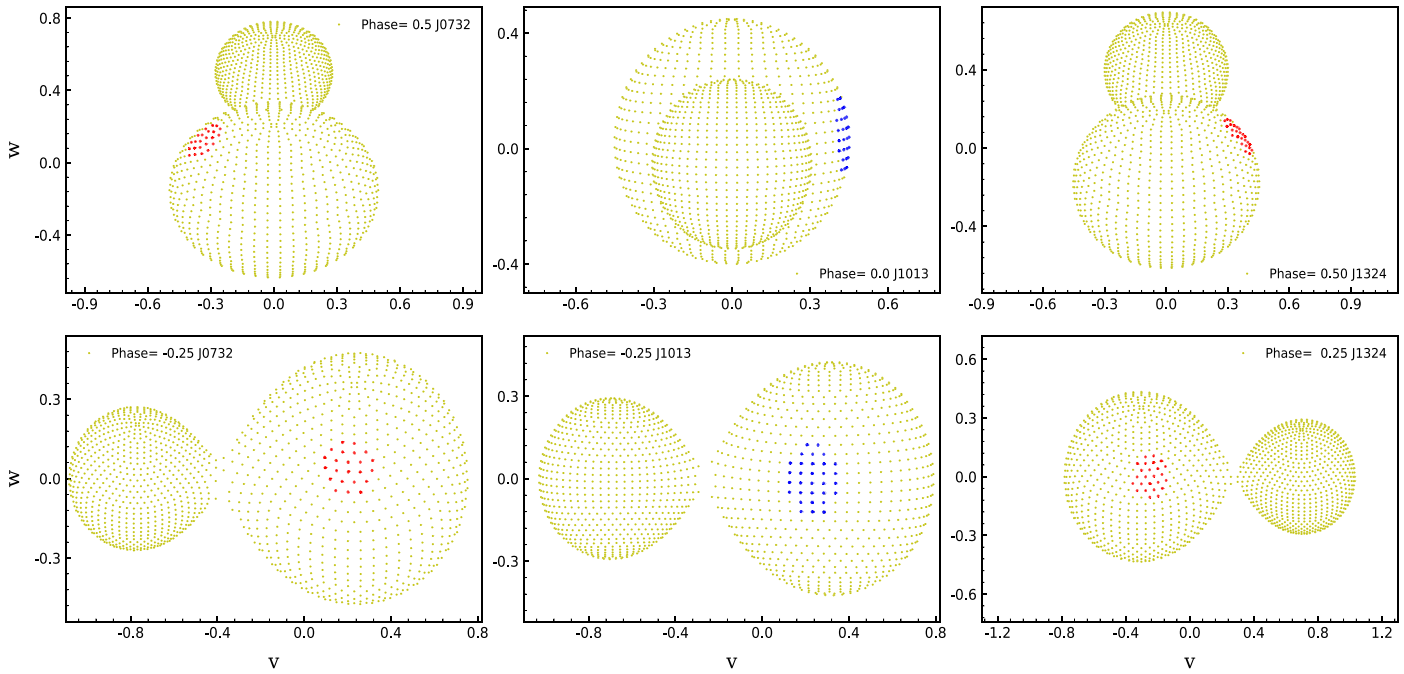

Figure 8. The spot distribution on surface of J0732 (left), J1013 (middle), and J1324 (right) on two different orbital phases (top and bottom). Both the hot and cool spots are shown by the blue and red regions, respectively.

$(r_{\rm pole} \times r_{\rm side} \times r_{\rm back})^{1/3}$. The synthetic LCs along with the observed LCs are shown in Figure 7. The spot distributions on the surface of J0732, J1013, and J1324 are shown in Figure 8.

5. Physical Parameters

The physical parameters, semimajor axis (A), mass of each component (M_1, M_2), radius of components (R_1, R_2), and luminosity of components (L_1, L_2) were determined using the photometric solutions and GAIA parallax as explained by Kjurkchieva et al. (2019). The adopted steps are given below:

(1) The peak apparent magnitude (m_v) was determined by Gaussian fitting around the phase $-0.25/0.25$ of the CRTS V-band LC. With the help of GAIA parallax (π), extinction (A_V), and the BC (different for each system due to different temperature, surface gravity, and metallicity), apparent magnitudes were converted to the bolometric magnitudes ($M_{\rm bol}$).

(2) The total luminosity ($L_T = L_1 + L_2$) of the system was determined from $M_{\rm bol}$. As the luminosity ratio was already available from LC modeling, it was used to determine the luminosity of individual components.

(3) For determining A, we assumed general luminosity-temperature-radius relation i.e., $L_i \propto T_i^4 \times R_i^2$. The relative radii of each component (r_i) was determined by PHOEBE in units of A. With the help of L_i, r_i , and T_i, A was determined. The radius of each component was determined by $r_i \times A$.

(4) Kepler's third law was used to find the total mass (M_T) of the system by using the period (P) and A. The primary and secondary masses were determined using q. The detailed procedure and equations involved in the parameter determination can found in Liu et al. (2020) and Panchal & Joshi (2021). The physical parameters for all the systems are given in Table 7. The values in parenthesis are the associated errors in the last digits.

We collected the parameters of EWs that were derived using photometric and spectroscopic observations from the literature (e.g., Deb & Singh 2011; Yildiz & Doğan 2013).

Table 7
The Absolute Parameters for the Five Systems Studied in the Present Work.

Parameters	J0158b	J0732	J1013	J1324	J1524
A ($R_\odot$)	2.12(4)	2.29(8)	1.75(4)	2.06(4)	1.86(5)
M_1 ($M_\odot$)	1.08(6)	1.5(2)	0.81(6)	1.16(7)	1.04(6)
M_2 ($M_\odot$)	0.77(4)	0.45(5)	0.36(3)	0.51(3)	0.41(2)
R_1 ($R_\odot$)	0.89(2)	1.13(4)	0.81(2)	0.93(2)	0.88(2)
R_2 ($R_\odot$)	0.76(1)	0.66(2)	0.56(1)	0.64(1)	0.57(1)
L_1 ($L_\odot$)	0.65(1)	1.13(6)	0.354(4)	0.49(1)	0.54(1)
L_2 ($L_\odot$)	0.36(1)	0.37(2)	0.184(2)	0.33(1)	0.201(3)

These well-characterized systems as well as the present results are plotted in M–L and M–R diagrams. It can be seen in Figure 9 that the primary components of subtype-W and -A EWs are close to the zero-age main-sequence (ZAMS) line. The secondaries of subtype W are more distant to the ZAMS line as compared to the secondaries of subtype-A systems. The structure and evolution of secondaries is different from those of the the primaries. The secondaries of J0732, J1013, J1324, and J1524 are more luminous than their main-sequence equivalents. Both components of J0158b are close to the ZAMS. The present targets follow a similar trend as that followed by other well-studied EWs.

6. Mass Transfer Rate

The period analysis performed in Section 3 shows that the systems J1013 and J1524 exhibit a change in $P_{\rm orb}$. Although there are different processes that can affect the orbital period, mass transfer between the components is the prime reason in most cases. The effect of processes like gravitational wave radiation (GWR) on the orbital period is usually very small. For J1013, the possible orbital period change due to GWR is estimated to be -2.631×10^{-16} days yr^{-1}, while the observed rate of change of period is -2.552×10^{-7} days yr^{-1}. Similarly, the orbital period changes that can occur due to magnetic

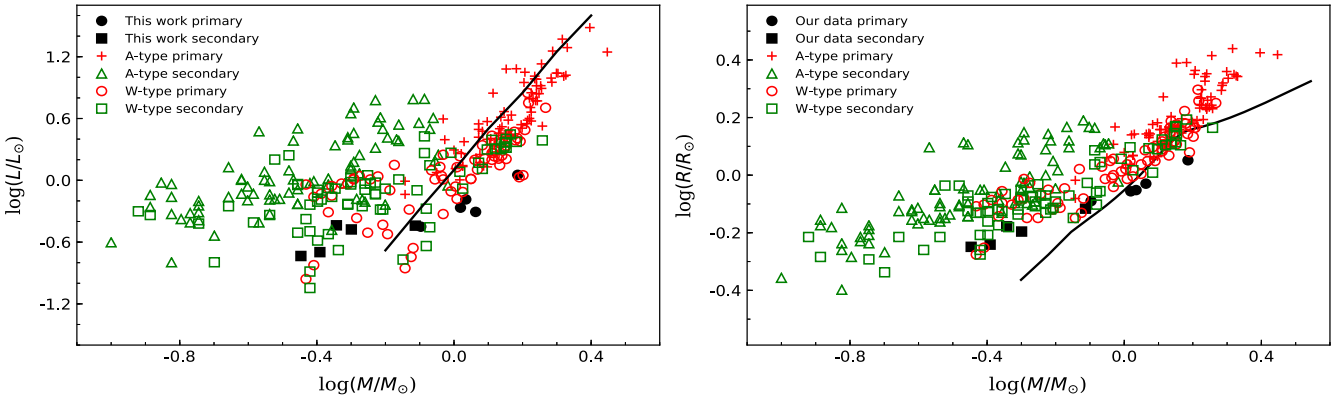

Figure 9. *M–L* and *M–R* relation for subtype-W and A EWs. The black continuous line is the ZAMS for $Z = 0.014$. The systems studied in the present work are shown in filled black circles (primary components) and squares (secondary components).

braking is found to be -4.035×10^{-8} days yr^{-1}. The orbital period change due to the magnetic braking is almost 16% of the observed change in J1013. The expected orbital period change due to GMR and magnetic braking is estimated as -3.533×10^{-16} and -5.130×10^{-8} days yr^{-1}, respectively, in the case of J1524. Hence, for J1524, the orbital period change due to the angular momentum loss via magnetic braking is almost 76% of the observed orbital period change rate. Therefore, in this system, magnetic braking as well as mass transfer between components could be responsible for the detected orbital period change. With the help of the mass transfer equation given by Kwee (1958), we determined the yearly rate of change of the mass of the primary components of J1013 and J1524. It was found that a -2.199×10^{-7} $M_{\odot}$ yr^{-1} rate of change of the mass of the primary component of the system J1013 can explain the observed orbital period change. Similarly, a rate of change of the mass of the primary component of -6.151×10^{-8} $M_{\odot}$ yr^{-1}, in the case of J1524, was determined to account for the observed orbital period change. Hence, the mass may be transferring from the primary to the secondary component in both components.

7. Chromospheric Activities

The magnetic activities, as shown by the Sun (Sun spots, solar flares, plages, coronal mass ejection, etc.) are also observed in late-type stars. These events are due to the stellar magnetic dynamo mechanism, which results from the differential rotation in the interior of the star. Phenomena like tidal forces, spinning and orbital synchronicity, and magnetic field interactions make things complex in the case of close interacting binaries. Close binary systems like RS CVn and BY Dra show observational evidence of chromospheric emission and magnetic field. Vogt (1981) studied II Peg using multiband photometric and low-resolution spectroscopic data and found that the strength of Hα was correlated to the spot visibility. The active close binaries show emission in the Ca II and Hα regions of their spectra. The components of active binary systems show stronger emission as compared to the single stars with the same rotational period (Montes et al. 1995). The level of activity can be inferred by emission or filled-in absorption lines in these wavelength regions. The H and K emission lines are primarily seen in K and M stars but they are not very common in F stars (Linsky 1980). The contribution of flux due to the active chromosphere can be determined by the removal of the photospheric flux from the total flux of a system. It is very hard to estimate the contribution of individual stars in the active chromosphere in the case of binary systems. The level of emission or filled-in absorption of one star can be altered due to its active/inactive companion (Montes et al. 1995). Such complications can be eliminated by the use of the spectral subtraction technique. It assumes that the photospheric and chromospheric flux contributions are independent of each other, which is applicable only to the localized active regions (Barden 1984; Huenemoerder & Ramsey 1984).

The low-resolution spectra for all the targets and appropriate inactive comparison stars spectra (with spectral class similar to the target stars) selected from available catalogs (Montes et al. 1999; Strassmeier et al. 2000; Valdes et al. 2004) were downloaded from the LAMOST website. All the spectra were normalized before analysis. The program STARMOD was used for building a synthetic spectra from two inactive comparison stars. With the help of STARMOD, different pairs of comparison stars were tested as primary and secondary components. The best pair was selected on the basis of minimum χ^2 determined by STARMOD after comparing the synthetic and observed spectra. The template spectra were constructed for J0158 (G7-star HD 237846 + G8-star BD +39 2723), J0732 (G7-star HD 86873 + G5-star HD 15299), J1013 (K3-star HD 219829 + G9-star BD +12 2576), J1324 (K1-star HD 233826 + G9-star BD +12 2576), and J1524 (G7-star HD 237846 + G8-star BD +39 2723). Figures 10 and 11 show the observed, synthetic, and subtracted spectra for all the targets. The figures only show the Hα region of spectra as the Ca II H and K, and Ca II infrared triplet wavelength regions of the spectra have a low S/N. Although a small amount of excess emission can be seen in all the subtracted spectra it should be noted that J0158b, J1324, and J1524 are the only sources with an S/N greater than 100 as given in Table 3. Due to the low spectral resolution and closeness of the two components, the observed spectral features are a blend of both components. Hence, it is impossible to detect the activity level of individual components and high-resolution spectroscopic observations are required for this purpose.

8. Results and Discussion

Photometric time series in different bands for five EWs were analyzed along with low-resolution spectroscopic data. The photometric time series data were collected from all previously available surveys to detect possible changes in their orbital period $P_{\rm orb}$. For three of the systems (J0158b, J0732, and J1324),

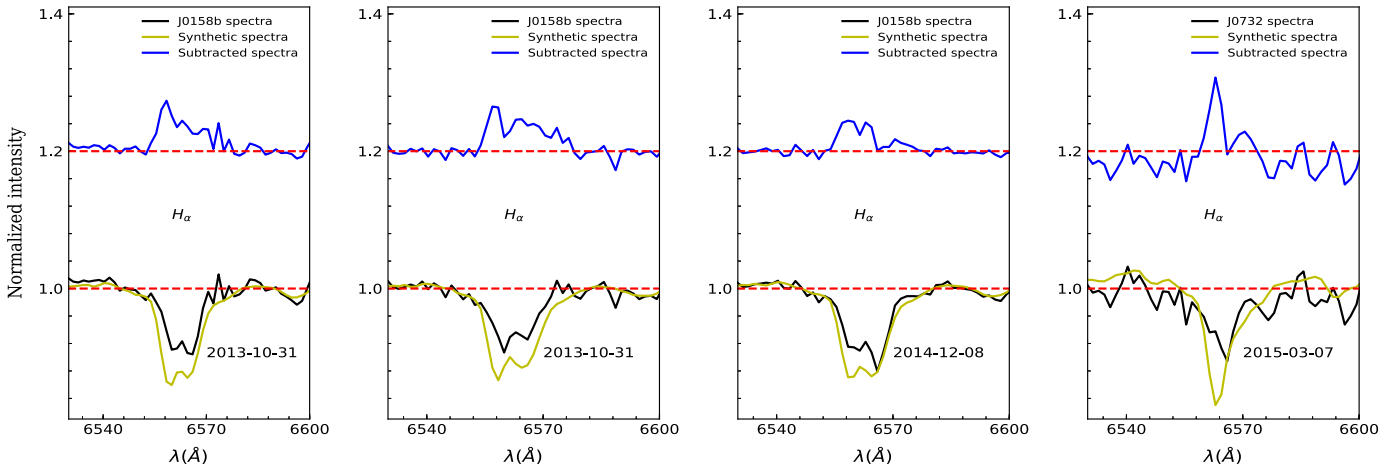

Figure 10. The Hα region of low-resolution LAMOST spectra (black line) and synthetic spectra (yellow line) for J0158b and J0732 are shown. The subtracted spectra in the same region is shown by a continuous blue line in each plot.

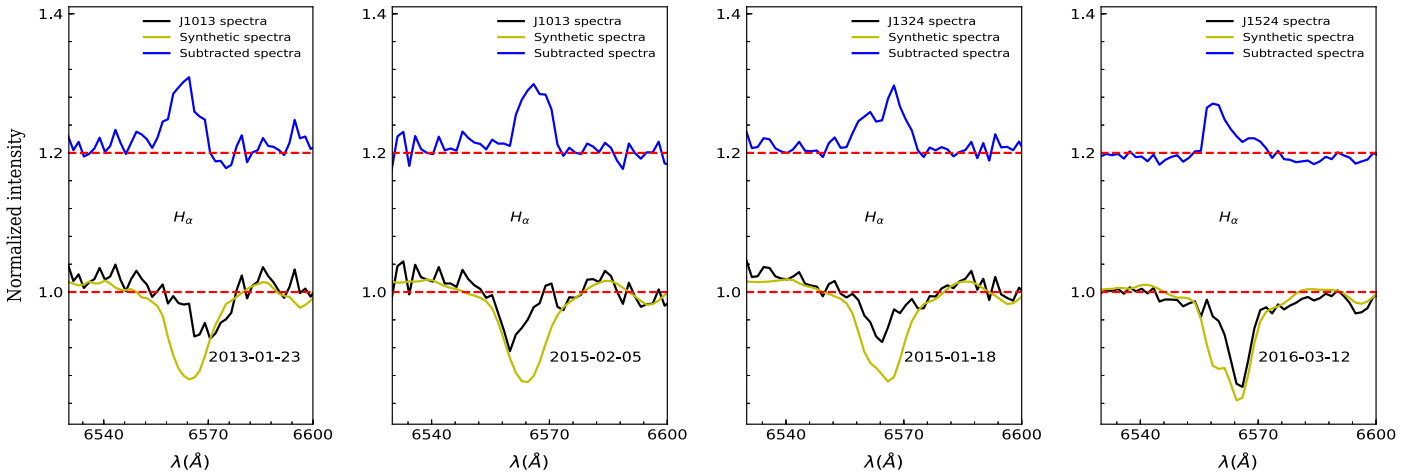

Figure 11. Same as in Figure 10 but for J1013, J1324, and J1524.

we find no evidence for changes in their $P_{\rm orb}$ in the time span of the photometric observations (14–15 yr), while for J1013 and J1524, the $P_{\rm orb}$ changes are evident. The possible contribution to this orbital period change rate on the basis of different processes was calculated. For J1013, the most plausible mechanism was found to be mass transfer from the primary to the secondary component, while the expected period rate due to magnetic braking angular momentum loss amounts to ∼16% of the observed period change rate. In the case of J1524, mass transfer and/or magnetic braking angular momentum loss can be responsible for the changing period. On the basis of the calculated semimajor axis, mass, and radii, it was found that possible magnetic braking angular momentum loss can cause up to 78% of the observed orbital period change rate.

For the LC modeling, the PHOEBE software was used and input parameters (like gravity darkening coefficients, surface albedos, and limb darkening coefficients) were chosen on the basis of temperature and convective envelope systems. The temperature can be determined on the basis of color–temperature relations but it can slightly deviate from the actual value if the color of the system is determined at different phases. Also, the temperature is a very important property as it is used to determine A, M_T, R_i, etc. Therefore, to get a better estimate of the temperature of the primary component, different methods were applied and the average of all the results was taken as the final $T_1^{\rm eff}$ value. We used the model for an over contact binary not in thermal contact in PHOEBE and the q-search technique to determine the mass ratio. The final parameters and errors are determined using the MCMC sampler with PHOEBE. To check the stability of the derived parameters, the parameter space around these solutions was scanned. For 625 models in the (q–i), (q–f), and (i–f) parameter spaces, an iteration process was used and the best solution was derived. The results showed that the adopted solutions have a lower cost function value than that of most of the surrounding region. According to the best-fit model, the temperature difference between the primary and secondary components was found to vary from 50 K to a few hundred Kelvin for all the systems. In the observed LCs, the depth of primary and secondary minima is different for each system. The massive and bigger components are fixed as a primary component. On the basis of the classification by Binnendijk (1970), the systems J0158 and J1524 were classified as subtype A, while others are subtype-W EWs. Only J0158 was found to have mass ratio q above 0.5. The fill-out factor f was below 25% for all the systems, so they are all classified as shallow-contact-type EWs.

The trustability of photometric mass ratios is an important subject. Although a q search using only photometric data is not as accurate as RV methods, it is used in almost every study where RV observations are unavailable. Terrell & Wilson (2005) showed that the photometric mass-ratio accuracy decreases as the system geometry changes from full eclipse to partial eclipse. Among 101 systems (59 total eclipsing and 42 partially eclipsing) collected by Li et al. (2021), almost half of the partial eclipsing binary photometric mass ratios were found to differ from the ones determined from RV curves. The mismatch was as big as 0.4 in some cases where the orbital inclination angle was less than 70°. In the present study, J1013 is the only system showing complete eclipses. Two of the other systems (J0158b and J1524) have $i > 70°$, while the the orbital inclination angle of J0732 and J1324 is below 60°. Hence, the mass ratio and other parameters should be considered as less reliable for the latter systems. The available TESS data was also modeled using the q value determined from the DFOT photometric data. The LCs of J0732 and J1013 are asymmetric around phases −0.25 and 0.25, so we included a cool or hot spot on one of the components for LC modeling. As the DFOT LC of J1324 appears to be symmetric, while the TESS LC shows clear asymmetries, we only included a spot for the modeling of the TESS data. Spot formation is quite common in contact binaries, especially for subtype-W EWs, which are found to be more active than those of subtype A. The spots can form and disappear on the stellar surface from time to time and their lifetimes can vary from days to years. Therefore, it is plausible that no spots are seen in the DFOT observations, while there appears to be one in the TESS data as the time of observation differs by approximately 9 months. For the determination of the physical parameters of EWs, we used general relations like the luminosity-radius-temperature relation and Kepler's third law. As GAIA DR3 provides an extraordinarily precise parallax for these systems and the LC parameters available through LC modeling, the physical parameters of the components can be determined easily using these relations. Other methods involve the use of empirical relations derived from a small sample of well-studied EWs. Therefore, such relations are highly dependent on the sample. The masses and luminosities of the individual components of the systems that we investigated show that the secondaries of all the systems are more luminous and bigger in size than mass-sequence stars of similar masses. As luminosity and mass can be transferred from one component to the other, the position of the components can deviate from the ZAMS. Energy transfer is still under debate, as which part of the convective envelope is involved in this process has not been confirmed yet.

The LAMOST spectra were used to search excess emission in the spectra. Only the region of Hα could be used for this exercise. Some random peaks were observed in the subtracted spectra of all the sources but the low resolution of the LAMOST spectra prevents the estimation of the contribution of the individual components. The small excess emission peaks in the subtracted spectra of J0732 and J1013 could be noise features because the S/N of their LAMOST spectra is rather low (S/N < 100). If we assume the emission features of the other systems are real, then J1524 and J1324 are likely to be more active than J0158b. Time series of high-resolution spectroscopic observations would allow confirming or rejecting the suspected excess emission peaks observed in these systems and help in the calculation of the contribution of the individual components.

This work is supported by the Belgo-Indian Network for Astronomy and astrophysics (BINA), approved by the International Division, Department of Science and Technology (DST, Government of India; DST/INT/BELG/P-09/2017) and the Belgian Federal Science Policy Office (BELSPO, Government of Belgium; BL/33/IN12). This publication makes use of VOSA, developed under the Spanish Virtual Observatory project supported by the Spanish MINECO through grant AyA2017-84089. VOSA has been partially updated by using funding from the European Union's Horizon 2020 Research and Innovation Programme, under Grant Agreement No. 776403 (EXOPLANETS-A). Guoshoujing Telescope (LAMOST) is a National Major Scientific Project built by the Chinese Academy of Sciences. Funding for the project has been provided by the National Development and Reform Commission. LAMOST is operated and managed by the National Astronomical Observatories, Chinese Academy of Sciences. In this work, we have also used data from the European Space Agency (ESA) mission GAIA, processed by the GAIA Data Processing and Analysis Consortium (DPAC). This work also make use of the 2MASS and SIMBAD databases.

Software: IRAF (Tody 1986, 1993), DAOPHOT (Stetson 1992), PERIOD04 (Lenz & Breger 2004, 2005), PHOEBE v1 (Prša & Zwitter 2005).

Appendix

Figures 12 and 13 show correlations and the posterior distributions of five parameters for each source.

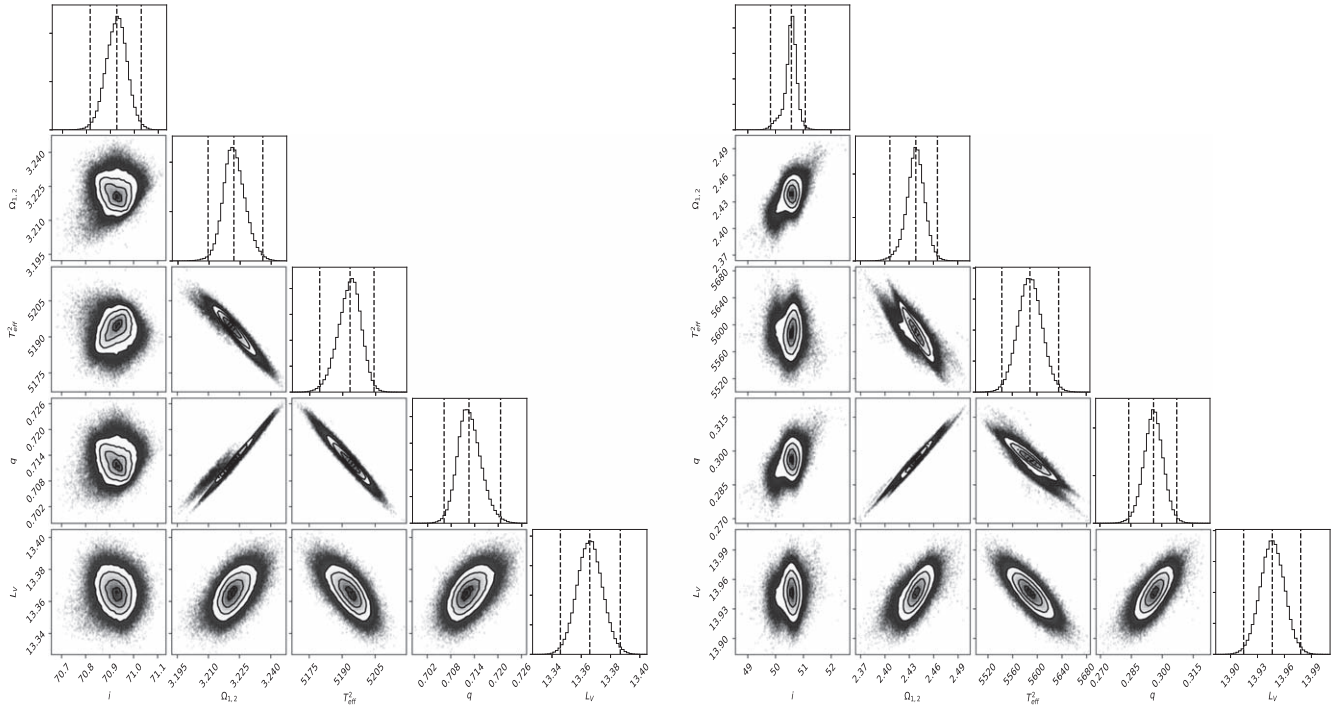

Figure 12. Corner plots for J0158 (left) and J0732 (right) showing the posterior distributions and the parameter correlations.

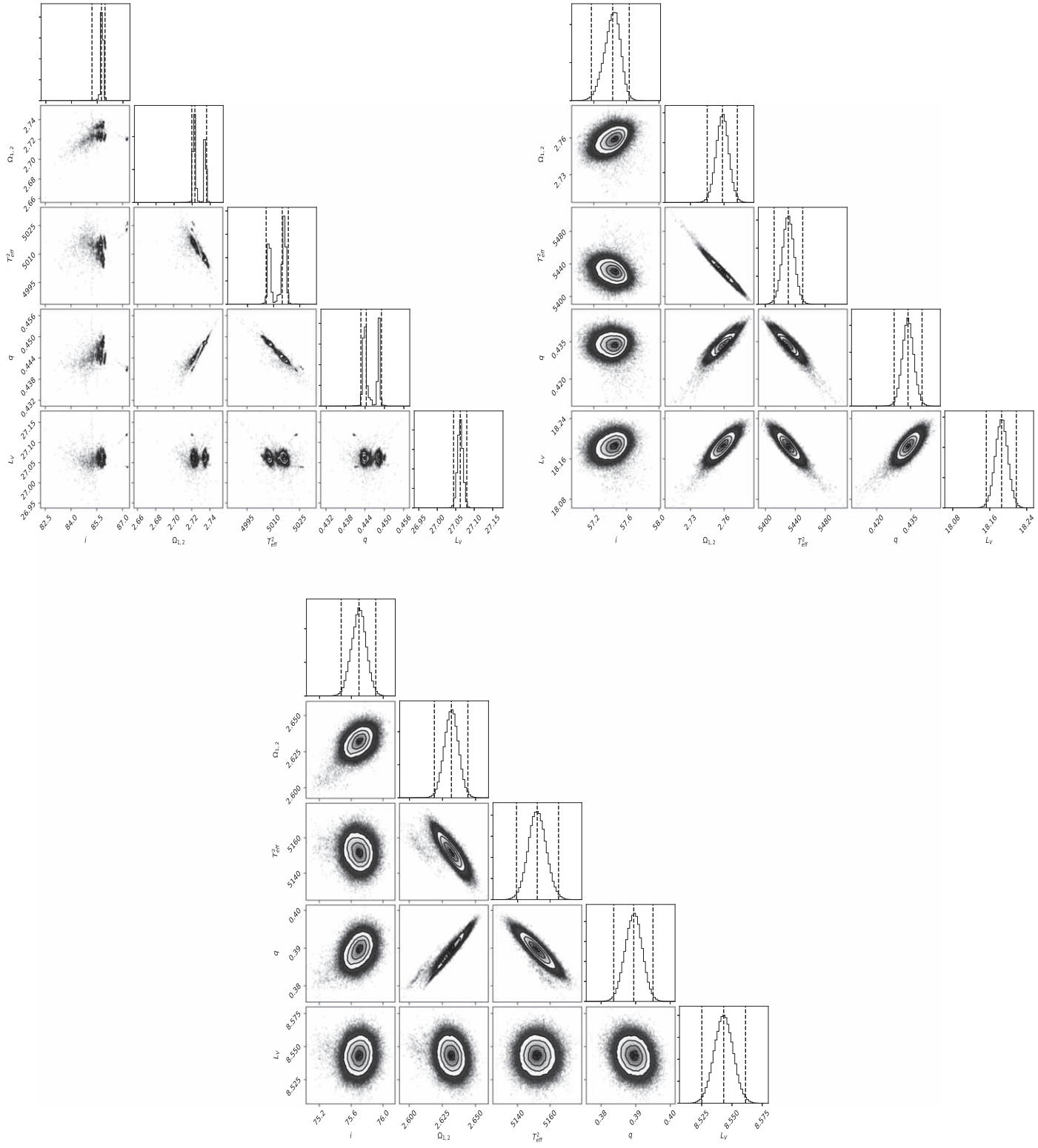

Figure 13. Same as Figure 12 but for J1013 (upper left), J1324 (upper right), and J1524 (lower).

ORCID iDs

Y. C. Joshi https://orcid.org/0000-0001-8657-1573
Peter De Cat https://orcid.org/0000-0001-5419-2042

References

Akerlof, C., Amrose, S., Balsano, R., et al. 2000, AJ, 119, 1901
Barden, S. C. 1984, BAAS, 16, 893

Bayo, A., Rodrigo, C., Barrado Y Navascués, D., et al. 2008, A&A, 492, 277
Bellm, E. 2014, in Proc. of The Third Hot-wiring the Transient Universe Workshop (HTU-III), ed. P. R. Wozniak, et al. (Stanford, CA: Stanford University SLAC), 27
Binnendijk, L. 1970, VA, 12, 217
Butters, O. W., West, R. G., Anderson, D. R., et al. 2010, A&A, 520, L10
Collier Cameron, A., Wilson, D. M., West, R. G., et al. 2007, MNRAS, 380, 1230
Deb, S., & Singh, H. P. 2011, MNRAS, 412, 1787
Drake, A. J., Graham, M. J., Djorgovski, S. G., et al. 2014, ApJS, 213, 9
Eker, Z. 1999, TJPh, 23, 357
Eker, Z., Ak, N. F., Bilir, S., et al. 2008, MNRAS, 389, 1722
Foreman-Mackey, D., Hogg, D. W., Lang, D., & Goodman, J. 2013, PASP, 125, 306
Gaia Collaboration, Brown, A. G. A., Vallenari, A., et al. 2021, A&A, 649, A1
Goodman, J., & Weare, J. 2010, Commun. Appl. Math. Comput. Sci., 5, 65
Huenemoerder, D. P., & Ramsey, L. W. 1984, AJ, 89, 549
Joshi, Y. C., & Jagirdar, R. 2017, RAA, 17, 115
Joshi, Y. C., Jagirdar, R., & Joshi, S. 2016, RAA, 16, 63
Kjurkchieva, D. P., Popov, V. A., Eneva, Y., & Petrov, N. I. 2019, RAA, 19, 014
Kozai, Y. 1962, AJ, 67, 591
Kuiper, G. P. 1941, ApJ, 93, 133
Kwee, K. K. 1958, BAN, 14, 131
Lenz, P., & Breger, M. 2004, in IAU Symp. 224, The A-Star Puzzle, ed. J. Zverko, et al. (Cambridge: Cambridge Univ. Press), 786
Lenz, P., & Breger, M. 2005, CoAst, 146, 53
Li, K., Xia, Q.-Q., Kim, C.-H., et al. 2021, AJ, 162, 13
Li, L., Han, Z., & Zhang, F. 2004, MNRAS, 355, 1383
Li, L., Zhang, F., Han, Z., & Jiang, D. 2007, ApJ, 662, 596
Linsky, J. L. 1980, ARA&A, 18, 439
Liu, L., Qian, S., Li, K., et al. 2020, Ap&SS, 365, 71
Lucy, L. B. 1967, AJ, 72, 309
Lucy, L. B. 1968, ApJ, 151, 1123
Luo, A. L., Zhao, Y.-H., Zhao, G., et al. 2015, RAA, 15, 1095
Montes, D., de Castro, E., Fernandez-Figueroa, M. J., & Cornide, M. 1995, A&AS, 114, 287
Montes, D., Ramsey, L. W., & Welty, A. D. 1999, ApJS, 123, 283
O'Connell, D. J. K. 1951, MNRAS, 111, 642
Ofek, E. O., Laher, R., Surace, J., et al. 2012, PASP, 124, 854
Ofek, E. O., Soumagnac, M., Nir, G., et al. 2020, MNRAS, 499, 5782
Panchal, A., & Joshi, Y. C. 2021, AJ, 161, 221
Pollacco, D., Skillen, I., Collier Cameron, A., et al. 2006, Ap&SS, 304, 253
Prša, A., & Zwitter, T. 2005, ApJ, 628, 426
Qian, S. 2001, MNRAS, 328, 914
Ricker, G. R., Winn, J. N., Vanderspek, R., et al. 2015, JATIS, 1, 014003
Schlafly, E. F., & Finkbeiner, D. P. 2011, ApJ, 737, 103
Skrutskie, M. F., Cutri, R. M., Stiening, R., et al. 2006, AJ, 131, 1163
Stetson, P. B. 1992, in ASP Conf. Ser. 25, Astronomical Data Analysis Software and Systems I, ed. D. M. Worrall, C. Biemesderfer, & J. Barnes (San Francisco, CA: ASP), 297
Strassmeier, K. G., Washuettl, A., Granzer, T., Scheck, M., & Weber, M. 2000, A&AS, 142, 275
Terrell, D., & Wilson, R. E. 2005, Ap&SS, 296, 221
Tody, D. 1986, Proc. SPIE, 627, 733
Tody, D. 1993, in ASP Conf. Ser. 52, Astronomical Data Analysis Software and Systems II, ed. R. J. Hanisch, R. J. V. Brissenden, & J. Barnes (San Francisco, CA: ASP), 173
Valdes, F., Gupta, R., Rose, J. A., Singh, H. P., & Bell, D. J. 2004, ApJS, 152, 251
van Hamme, W. 1993, AJ, 106, 2096
van't Veer, F., & Maceroni, C. 1989, A&A, 220, 128
Vogt, S. S. 1981, ApJ, 247, 975
Watson, C. L., Henden, A. A., & Price, A. 2006, SASS, 25, 47
Wilson, R. E., & Devinney, E. J. 1971, ApJ, 166, 605
Yildiz, M., & Doğan, T. 2013, MNRAS, 430, 2029